

A Unique RGO Aerogel/TiO₂/MoS₂ Composite Photocatalyst with a 3D Sandwich Network for the Removal of Organic Dyes by the Cooperative Action of Adsorption and Photocatalysis

Yujuan Zhang

Xi'an University of Architecture and Technology

Haojie Qi

Xi'an University of Architecture and Technology

Liang Zhang (✉ zl98zl@hotmail.com)

Xi'an University of Architecture and Technology <https://orcid.org/0000-0002-4056-9803>

Yao Wang

Xi'an University of Architecture and Technology

Lvling Zhong

Xi'an University of Architecture and Technology

Yage Zheng

Xi'an University of Architecture and Technology

Xin Wen

Xi'an University of Architecture and Technology

Xiaomin Zhang

Xi'an University of Architecture and Technology

Juanqin Xue

Xi'an University of Architecture and Technology

Research Article

Keywords: absorption, photocatalysis, visible light, RGO aerogel, MoS₂, physical vapor deposition.

Posted Date: May 4th, 2021

DOI: <https://doi.org/10.21203/rs.3.rs-431756/v1>

License:  This work is licensed under a Creative Commons Attribution 4.0 International License.

[Read Full License](#)

Abstract

A unique composite with a three dimensional (3D) sandwich network structure consisting of reduced graphene oxide aerogel/titanium dioxide/molybdenum disulfide (abbreviated as RGO aerogel/TiO₂/MoS₂) was developed for the removal of organic dyes from solution cooperatively by adsorption and photocatalytic degradation mechanisms. The composite was successfully synthesized by stepwise hierarchical assembly integration, including sol-gel and physical vapor deposition (PVD) methods. The resulting multicomponent composite material featured a high specific surface area (255.441 m²/g) absorption capacity manifested by the myriad negatively charged carboxylate function groups on the surface of the composite. The composite material demonstrated ideal optical and photocatalytic properties, including a large absorbance in the visible light region and a fast transfer of photogenerated electron-hole pairs, resulting in a superb photodegradation performance. The RGO aerogel/TiO₂/MoS₂ also exhibited a high cationic dyes removal efficiency through the cooperative adsorption and photocatalytic degradation mechanisms. Moreover, electron paramagnetic resonance (EPR) analysis and reactive oxygen species scavenging experiments confirmed that superoxide radicals (O₂^{•-}), holes (h⁺), and hydroxyl radicals (•OH) were involved in photocatalytic degradation of the organic dyes.

Highlights

- RGO aerogel/TiO₂/MoS₂ composite was synthesized via the sol-gel and PVD methods.
- RGO aerogel/TiO₂/MoS₂ composite showed a unique 3D sandwich network structure.
- Rich oxygen-containing functional group and large specific surface area were showed.
- Synergy of adsorption and photocatalysis caused high removal efficiency of dyes.

1. Introduction

The continuously increasing activities of various chemical industries have led to a considerable amount of dye wastewater being produced from dyeing processes. Organic pollutants with complex structures present in these wastewater streams are extremely difficult to degrade. More importantly, they are highly toxic and represent a serious threat to the life of aquatic organisms and people (Li et al. 2017; Zhang et al. 2017). Therefore, researchers have begun to develop more effective methods to manage the production of dye-containing wastewater (Cai et al. 2017). Adsorption technologies represent a widely used method for treating wastewater because they enable high removal efficiencies of environmental pollutants, are economically produced, and do not require the use of secondary pollutants (Chen and Bai 2013; Martins et al. 2020; Yang et al. 2015). In addition, photocatalytic technology can degrade organic waste into low-toxicity or non-toxic, low-molecular-weight organic compounds under irradiation and can even decompose pollutants into carbon dioxide and water, which renders it a potentially environmentally friendly method for treating sewage (Guo et al. 2014; Wang et al. 2016; Zhang et al. 2015).

The combination of adsorption and photocatalytic technologies is promising because the cooperation between these two processes can achieve a better removal efficiency of organic dyes compared to their individual processes (Dursun et al. 2020; El Mersly et al. 2021; Zhang et al. 2020). Strong interactions between dye molecules and functional groups on the surface of a catalyst ensued from adsorption can facilitate rapid and efficient reactivity between dye molecules and short-lived reactive materials, such as reactive oxygen species (ROS), produced on photocatalyst surface, resulting in photodegradation (Martins et al. 2020). Upon photocatalytic degradation, the products are desorbed from the catalyst surface, regenerating the adsorption sites to assist in further dye removal (Guo et al. 2014; Luo et al. 2019). Titanium dioxide (TiO_2) has gained considerable interest as a photocatalytic material because of it is biocompatible, non-toxic, and does not produce secondary environmental pollutants. However, TiO_2 exhibits a high electron-hole pair recombination rate and a low solar energy utilization rate (Shi et al. 2017; Wang et al. 2014; Zhang et al. 2016).

To circumvent this, modifiers can be added into the structure of a photocatalyst. Molybdenum disulfide (MoS_2) has demonstrated excellent promise as a modification for photocatalysts (Li et al. 2018). In the visible light range, the heterojunction formed between TiO_2 and MoS_2 can accelerate the separation of photoexcited electrons and holes, prolonging the life of an electron (Hu et al. 2019; Liu et al. 2017; Wang et al. 2018). The most widely used method for incorporating MoS_2 into other materials is by hydrothermal synthesis using various MoS_2 precursors (Liu et al. 2017; Wang et al. 2018). However, these MoS_2 -containing nanomaterials are prone to agglomeration on the carrier materials, which can break the special structure of the carrier materials when combined by this method. The physical vapor deposition (PVD) approach has the potential to immobilize MoS_2 nanomaterials on surface of the carriers because the material deposited by this method becomes uniformly distributed across the carrier surface, and the carrier micropore structure has little influence on this process due to the use of gases as precursors (Feng et al. 2015; Zhou et al. 2016).

Recently, three-dimensional (3D) carbon materials, such as aerogels, have been considered promising adsorbents because they are non-toxic and have a large specific surface area (Xin et al. 2019; Yang et al. 2019). Reduced graphene oxide (RGO) aerogels contain numerous carboxylic acid functional groups throughout its 3D network structure, which become negatively charged in aqueous solution, promoting the absorption of cationic organic dyes by electrostatic and hydrogen bonding interactions. The RGO aerogels also possess larger specific surface areas with myriad active sites, which not only enables the exposure of the catalyst to more dye molecules to facilitate their removal but also offers additional attachment points for the photocatalyst. Moreover, the RGO aerogel can efficiently absorb photons to promote the photoexcitation of electrons (Li et al. 2016) and features multi-dimensional electron migration paths that facilitate the migration of photoexcited electrons (Qiao et al. 2019).

In this paper, a RGO aerogel/ TiO_2 / MoS_2 composite photocatalyst featuring a 3D network sandwich structure was prepared using sol-gel and PVD methods and evaluated for its removal efficiency of organic dyes from dye-containing solutions. A high removal efficiency of the various cationic organic

dyes tested herein was obtained through cooperative adsorption and photocatalytic degradation mechanisms. These results indicated that the composite had broad application prospects in the treatment of dye-containing wastewater.

2. Experimental

2.1 Materials and reagents

Molybdenum disulfide (MoS_2) was obtained from the Fuchen Chemical Reagents Plant (Tianjin, China). Tetrabutyl titanate was provided by Sanpu Chemical Co., Ltd. (Shanghai, China). Crystalline flake graphite was derived from Tengshengda Carbon Machinery Co., Ltd. (Qingdao, China). The organic dyes Rhodamine B (RhB), crystal violet (CV), methylene blue (MB), Alizarin red (AR), xylenol orange (XO), and methyl orange (MO) were obtained from Kermel Chemical Reagent Co., Ltd. (Tianjin, China) and were of analytical grade. These materials were used as is without purification or treatment. Deionized (DI) water was used as the solvent for all solutions and experiments.

2.2 Preparation of the RGO aerogel/ TiO_2 / MoS_2 composite

The RGO aerogel/ TiO_2 / MoS_2 composite was synthesized via the sol-gel and physical vapor deposition (PVD) methods. First, graphene oxide (GO) was prepared by Hummers' method and treated by freeze-drying. The resulting aerogel GO (0.4 g) was added to 20 mL of absolute ethanol, and the mixture was ultrasonically exfoliated at room temperature for 2 hours. Then, 1.5 mL of tetrabutyl titanate was dispersed into the mixture, and 3 mL of DI water was added. The precipitate was washed with DI water and treated via freeze-drying to obtain the RGO aerogel/ TiO_2 .

MoS_2 (0.5 g) was added to a ceramic boat that was then wrapped with aluminum paper and tied with several holes. The ceramic boat and 1.0 g of the RGO aerogel/ TiO_2 composite were placed in a reactor and heated at 570°C for 3 hours at a heating rate of $5^\circ\text{C}/\text{min}$, after which they were cooled to room temperature and removed from the reactor to obtain the final RGO aerogel/ TiO_2 / MoS_2 composite material. The RGO aerogel/ TiO_2 was prepared the same way but without adding MoS_2 .

2.3 Characterization methods

X-ray diffraction (XRD, Bruker D8 Advance X-ray diffractor, Karlsruhe, Germany) using Cu K α radiation was performed on the RGO aerogel/ TiO_2 / MoS_2 composite material to determine the crystal phase structure. Raman spectroscopy (LabRAM HR Evolution) with an excitation of 532 nm was performed to determine the phase composition of the composite material. A survey of the chemical bonds and functional groups within the material was conducted by fourier transform infrared spectroscopy (FT-IR, Nicolet iS50 FT-IR spectrometer). The morphology, size, and microstructural properties of the composite were investigated by scanning electron microscopy (SEM, Verios 460) and transmission electron microscopy (TEM, Tecnai G2 F20). X-ray photoelectron spectroscopy (XPS, ESCALAB 250Xi) with Al K α radiation ($h\nu = 1486.6$ eV) was performed to determine the elemental composition of the composite

material. To assess the incorporation of MoS₂ into the material, the sample was characterized by energy-dispersive X-ray spectroscopy (EDS), as shown in Fig. S1. Ultraviolet-visible diffuse reflectance spectroscopy (UV-Vis DRS, Shimadzu UV2600 UV-Vis spectrophotometer) was applied for studying the light absorption properties of materials.. The recombination rate of the photogenerated electron-hole pairs was determined using photoluminescence (GangDong F-320 fluorescence spectrophotometer). The Brunauer-Emmett-Teller (BET) surface areas, pore volumes, and pore size distributions of the materials were measured using an ASAP 2460 surface area and porosity analyzer (Micrometrics Instrument Corp.). Electron paramagnetic resonance (EPR) spectroscopy was conducted by an EMXmicro-6/1/P/L EPR spectrometer to identify the spin-trapped oxidative radical species. The spectrometer was equipped with a xenon lamp and a UV-cutoff filter ($\lambda \geq 400$ nm). The center magnetic field was set to 3500 G, the power was set to 6.35, and microwave frequency was 15 dB. The degradation intermediates of Rhodamine B (RhB) were analyzed by gas chromatography-mass spectrometry (GC-MS, Agilent 7890A/5975C).

2.4 Photodegradation of the organic dye solutions

We designed in-house a photocatalytic reaction device, a photo of which is shown in Figure S6. Up to 10 sets of samples were able to be placed at equal distances around the device. The light source of the device was set in the center of the device, the dye solution was placed in a quartz test tube, with the distance between the light source and the dye solution being 6 cm. An air pump was used for gas stirring. circulating air was used for cooling. Took samples while stirring, so that the ratio of solution to catalyst remained unchanged, and the sample did not return to the main solution. A certain amount of the photocatalyst was dispersed into an organic dye standard solution. Upon reaching adsorption-desorption equilibrium between the dye and the photocatalyst, the suspensions were continuously stirred in the dark for 30 min. After the suspension was centrifuged, it was measured by UV-vis spectroscopy (722G UV-vis spectrophotometer, Shanghai Chuang Yi Science & Education Equipment Co., Ltd.) The mixed suspensions were irradiated using a high-pressure sodium lamp (HPSL, 278 W/m² intensity), in the intervals of illumination 3 ml suspension every 30 min was withdrawn and centrifuged to remove the photocatalyst particles for measurement. The removal efficiencies of the organic dyes were obtained using Eq. 1 below:

$$D \% = (C_0 - C_t) / C_0 \times 100 \% \quad (1)$$

where C_0 was the initial concentration, and C_t was the concentration at time t .

The photodegradation kinetics of the dyes were fitted with the Langmuir-Hinshelwood pseudo-first-order kinetic equation (Eq. 2):

$$\ln (C_0 / C_t) = k_{app}t \quad (2)$$

where C_0 was the adsorption-desorption equilibrium concentration, C_t was the concentration at time t , and k_{app} was the apparent constant (Guo et al. 2014)

3. Results And Discussion

3.1 Characterization

3.1.1 Structures and morphological characterization

The XRD patterns of the RGO aerogel/TiO₂/MoS₂ composite included Bragg reflections of anatase TiO₂, which corresponded to the JCPDF powder diffraction pattern 21-1272 (Guo et al. 2014; Wang et al. 2014). The (002), (100), and (103) crystal planes presented in Fig. 1A matched well with the diffraction peak of MoS₂ (JCPDF 37-1492), confirming the coexistence of MoS₂ in the composite material. The XRD patterns of the MoS₂ (Fig. 1A) had lower diffraction peak intensities than TiO₂, which was ascribed to the lower proportion of MoS₂ in the RGO aerogel/TiO₂/MoS₂ (Ye, Fei et al. 2017). Due to the lower intensity of the RGO diffraction peak, no obvious diffraction peaks corresponding to the carbon materials in the RGO aerogel/TiO₂/MoS₂ were observed (Qiao et al. 2019).

To further explore the physical properties of the RGO aerogel/TiO₂/MoS₂ material, Raman spectroscopy was performed. The Raman spectrum in Fig. 1B showed several peaks at 141.95 cm⁻¹, 512.61 cm⁻¹, and 632.78 cm⁻¹ that were characteristic of the E_{g(1)}, A_{1g}, and E_{g(2)} modes of anatase TiO₂. The characteristic peaks observed at 378.32 cm⁻¹ and 410.31 cm⁻¹ corresponded to the E_{2g} and A_{1g} modes of MoS₂. The two peaks at 1344.39 cm⁻¹ (D band) and 1599 cm⁻¹ (G band) corroborated the existence of RGO in the RGO aerogel/TiO₂/MoS₂ composite (Paul et al. 2018; Qiao et al. 2019). Moreover, because the RGO aerogel featured a significant amount of carboxylic acid functional groups in its structure, the resulting composites prepared with the RGO aerogel (i.e. RGO aerogel/TiO₂ and RGO aerogel/TiO₂/MoS₂) displayed similar FT-IR spectral characteristics (Fig. 1C). In each of the three materials analyzed (RGO, RGO/TiO₂, and RGO/TiO₂/MoS₂) the corresponding FT-IR spectra featured absorption peaks corresponding to the stretching vibrations of O-H at 3600–3200 cm⁻¹, C-H at 3057–2790 cm⁻¹, C-O at 1344–930 cm⁻¹, and C = O/C = C at 1750–1344 cm⁻¹. However, the RGO/TiO₂ and RGO/TiO₂/MoS₂ materials both featured strong and weak, respectively, absorption bands at 769–410 cm⁻¹, which correspond to the Ti-O-C/Ti-O-Ti stretching vibrations, which further corroborated the incorporation of TiO₂ into the material (Wang et al. 2013; Wang et al. 2017). However, these absorption bands were not present in the FT-IR spectrum of the plain RGO aerogel.

Next, the morphologies and structures of both the RGO aerogel and the RGO aerogel/TiO₂/MoS₂ composite were investigated via SEM and TEM (Fig. 2).

The SEM image of the RGO aerogel indicated a 3D hierarchical network structure with an interlayer distance equal to dozens of nanometers (Fig. 2A). Upon the incorporation of TiO₂ and MoS₂ into the RGO aerogel, the interlayer distance of the RGO aerogel sheets in the RGO aerogel/TiO₂/MoS₂ increased (Fig. 2B), which was conducive to the adsorption of more dye molecules. The thickness of the graphene was approximately 30 nm, and the 3D network structure demonstrated clear pores that would effectively enable the adsorption of the organic dyes. The TiO₂ nanoparticles (NPs), which had sizes of

approximately 20 nm, were uniformly layered on the graphene sheet, so that more active sites were exposed, which was conducive to facilitating more efficient photocatalysis compared to when fewer active sites were exposed. In addition, the material was highly crystalline, which was consistent with the XRD results.

During the preparation of TiO_2 using the sol-gel method, the interactions between the TiO_2 precursors and the GO sheets were strong. However, the interactions between the individual GO sheets were weak, resulting in an increased interlayer distance (Wang et al. 2013) The TiO_2 NPs were uniformly coated on the surface of the RGO aerogel sheets, which was consistent with the TEM image presented in Fig. 2C. The MoS_2 was barely observed in the SEM image, which might have been due to the low proportion of MoS_2 compared to the other components of the composite. Analysis of the composite by EDS indicated that the material had a significant amount of C, moderate amounts of Ti and O, and noticeably small amounts of S and Mo, which further indicated that the TiO_2 was uniformly coated on the RGO aerogel surface and that the MoS_2 layer was attached to the surface of the RGO aerogel/ TiO_2 composite.

The high-resolution TEM (HRTEM) image in Fig. 2D, which represents a zoomed-in picture of the red square area in Fig. 2C, also verified the presence of MoS_2 based on the 2–4 layered MoS_2 sheets attached on the surface of TiO_2 . The lattice spacing of 0.62 nm corresponded to (002) crystal plane, while the lattice spacing of the TiO_2 crystal (0.35 nm), which was represented by the yellow square area, corresponded to the (101) crystal plane (inset, Fig. 2D) (Li, Juan-Juan et al. 2018; Lin et al. 2019; Paul et al. 2018; Quan, Quan et al. 2018; Wang et al. 2013; Wang et al. 2017; Ye, Fei et al. 2017). Moreover, the interlayer distance of the RGO aerogel itself was 0.45–0.65 nm. The HRTEM in Fig. 2D also demonstrated the presence of clear and cohesive interfaces between the different components in the material. The results of these analyses, which determined the overall distribution of each material throughout the sample, denoted the formation of a sandwich structure produced by the stepwise hierarchical assembly integration method. The EDS elemental mapping results of the RGO aerogel/ TiO_2 / MoS_2 composite confirmed that the TiO_2 was uniformly present on the surface of the RGO aerogel and that the MoS_2 layer was adsorbed onto the surface of the RGO aerogel/ TiO_2 material.

3.1.2 Microstructure via XPS

The peaks corresponding to C 1s, Ti, O, Mo, and S in the XPS survey spectrum (Fig. 3A) were consistent with the elemental composition of the materials. The C 1s spectrum (Fig. 3B) displayed three main peaks at 284.47 eV, 286.37 eV, and 288.77 eV, which corresponded to the C-C/C = C, C-O, and C = O groups, respectively (Li, Juan-Juan et al. 2018; Quan, Quan et al. 2018). The O 1s spectrum shown in Fig. 3C displayed three peaks at 533.41 eV, 532.57 eV, and 530.69 eV, which were attributed to the C-O, Ti-O-C, and Ti-O-Ti groups, respectively; the Ti-O-C bond resulted from the strong interactions between the TiO_2 and the RGO aerogel (Li, Juan-Juan et al. 2018; Wang et al. 2017). The Mo 3d and S 2p spectra in Fig. 3D and E, respectively, featured peaks at 231.87 eV, 228.47 eV, 164.57 eV, and 163.37 eV, which corresponded to $\text{Mo } 3d_{3/2}$, $\text{Mo } 3d_{5/2}$, $\text{S } 2P_{1/2}$, and $\text{S } 2P_{3/2}$, respectively, that were attributed to the Mo^{4+} and S^{2-} species in

MoS₂, respectively (Quan, Quan et al. 2018). The Ti 2p spectrum presented in Fig. 3F featured two characteristic peaks corresponding to the Ti 2p_{1/2} and Ti 2p_{3/2} spin-orbital splitting photoelectrons of the TiO₂ in the RGO aerogel/TiO₂ and RGO aerogel/TiO₂/MoS₂ materials. The binding energy peaks at 458.48 eV and 464.16 eV represented the characteristic peaks of TiO₂. Upon the incorporation of TiO₂ into the GO structure following heat treatment, the respective peaks in the RGO aerogel/TiO₂ material shifted slightly to 459.05 eV and 464.8 eV, while these characteristic peaks in the RGO aerogel/TiO₂/MoS₂ shifted even more to 459.55 eV and 465.2 eV. These shifts were attributed to the formation of Ti-O-C bonds between the TiO₂ NPs and the RGO aerogel.

3.1.3 UV-Vis DRS and PL analysis

The optical absorption properties of the RGO aerogel, RGO aerogel/TiO₂, and RGO aerogel/TiO₂/MoS₂ materials were assessed by UV-Vis DRS. As shown in Fig. 4A (curve c), the pure RGO aerogel responded to visible light, while pure TiO₂ did not (Guo et al. 2014; Wang et al. 2018). The modification of the RGO aerogel with TiO₂ manifested a red shift and a strong absorption increase in the visible light region. However, the RGO aerogel/TiO₂/MoS₂ demonstrated the strongest visible light absorbance, as confirmed by the absorption spectra of the RGO aerogel/TiO₂/MoS₂ and RGO aerogel/TiO₂ materials in Fig. 4A (curves a and b, respectively). From these spectra, the band gap energy (E_g) values were obtained. The band gap energies of the RGO aerogel, RGO aerogel/TiO₂, and RGO aerogel/TiO₂/MoS₂ were 1.57 eV, 1.81 eV, and 1.76 eV, respectively. The enhancements in the visible light adsorption and the reduction in the optical band gap of the RGO aerogel/TiO₂ and RGO aerogel/TiO₂/MoS₂ materials compared to the neat RGO aerogel were attributed to Ti-O-C bonds at the interface of the TiO₂ and RGO aerogel (Wang et al. 2013).

The photoluminescence (PL) spectra of the titanium dioxide (P25), RGO aerogel, RGO aerogel/TiO₂, and RGO aerogel/TiO₂/MoS₂ materials at an excitation wavelength of 397 nm are presented in Fig. 4B. Lower PL intensities imply a lower recombination rate of the photogenerated electron-hole pairs compared to higher PL intensities (Guo et al. 2014; Wang et al. 2017). The PL intensity of the RGO aerogel/TiO₂ was lower than that of P25, the RGO aerogel/TiO₂/MoS₂ composite had the lowest PL intensity, which indicated the lowest recombination rate photogenerated electron-hole pairs compared to the other materials measured.

3.2. Application of dye removal

3.2.1 Effect of initial RhB concentration and pH on dye removal

The removal efficiency of the RGO aerogel/TiO₂/MoS₂ composite under HPSL irradiation was evaluated based on the change in initial RhB concentration (C_{RhB}), as shown in Fig. 5A. In a dark environment, as the initial RhB concentration increased, the RhB removal efficiency by the RGO aerogel/TiO₂/MoS₂

composite decreased. When the initial RhB concentration increased, more dye molecules were adsorbed onto the catalyst, but after the catalyst reached adsorption-desorption equilibrium, the concentration of dye molecules in the solution no longer changed. As the initial dye concentration increased, more dye molecules were excited by absorbed photons, which resulted in greater energy transfer during the photocatalytic degradation process, and adsorption sites were created to help remove the dye (Luo et al. 2019; Zhang et al. 2019). However, the high concentration of dyes at the surface of the catalyst caused the transfer of photons to the photocatalyst to be blocked by the absorption by the adsorbed dye molecules, reducing the number of photons reaching the catalyst surface (Guo et al. 2014). The corresponding photodegradation kinetics data of RhB at different concentrations were fitted to a pseudo-first-order model (Fig. 5B). The apparent constants calculated from the model (Table 1) indicated that the optimal rate constant (0.0169 min^{-1}) was achieved at an RhB concentration of 40 mg/L. At this concentration, the optimal removal efficiency of RhB was determined to be 95% after a duration of 150 min. This removal efficiency was achieved by the combination of adsorption and photocatalytic degradation.

The pH of the medium was also a factor to consider because it affected the adsorption capacity and photocatalytic performance of the composite (Chen and Bai 2013; Yahia Cherif et al. 2014). The removal of RhB from the corresponding RhB solutions at different pH's was performed by the RGO aerogel/TiO₂/MoS₂ composite (Fig. 5C). The adsorption capacity of the composite in the dark increased between pH 1.0 and 7.0 but decreased when the pH exceeded 7.0. Therefore, the optimal adsorption capacity was achieved at pH 7.0. The decreased removal efficiency of the composite photocatalyst at lower pH was attributed to the protonation of surface-active carboxylic acid groups, which prevented the adsorption of RhB molecules at the adsorption sites. As the pH increased, the functional groups on the catalyst surface became increasingly deprotonated, which enabled the binding of the cationic RhB molecules via electrostatic interactions. However, when the pH exceeded 7.0, the reduction in the adsorption capacity of the composite was due to the competition between the high concentration of hydroxide ions in solution and the RhB molecules for adsorption sites.

The photodegradation performance also demonstrated the same behavior as the adsorption capacity. The strong adsorption of the dyes onto the composite surface due to increased localized dye concentration enabled rapid and efficient collisions between the dye molecules and the reactive species (Guo et al. 2014; Luo et al. 2019). The corresponding photodegradation kinetics data of RhB at different pH's were also fitted to a pseudo-first-order model (Fig. 5D), and the calculated apparent rate constants are shown in the Table 1. From the comprehensive kinetics data, the optimal removal efficiency was achieved at a pH of 7, with a corresponding removal efficiency of 97 %.

Table 1
Apparent rate constants (k_{app}) and regression coefficients (R^2) of photodegradation at different initial RhB concentrations (C_{RhB}) and different pH's.

C_{RhB} (mg/L)	k_{app} (min^{-1})	R^2	pH	k_{app} (min^{-1})	R^2
20	0.0135	0.9998	1	0.0076	0.9874
40	0.0169	0.9997	3	0.0096	0.9740
60	0.0082	0.9876	7	0.0183	0.9985
80	0.0067	0.9879	9	0.0171	0.9985
100	0.0034	0.9994	11	0.0143	0.9901

3.2.2 Photocatalytic performance of the composite.

As shown in Fig. 6, the photocatalytic performance of RhB on the RGO aerogel, RGO aerogel/ TiO_2 , and RGO aerogel/ $\text{TiO}_2/\text{MoS}_2$ materials under HPSL radiation was evaluated. The adsorption-desorption curve of the composite material under dark adsorption in rhodamine B solution for 30 minutes is shown in Figure S3.

Due to a band gap energy of 3.2eV, the TiO_2 cannot absorb visible light (Shi et al. 2017). The pure RGO aerogel also had a weak photocatalytic performance. Compared to single-component photocatalysts, composite photocatalysts typically demonstrate higher photocatalytic performances. Therefore, the combination of the two components can effectively improve their own shortcomings. The RGO aerogel/ TiO_2 showed significantly enhanced photocatalytic activity because the absorption of visible light by the composite led to the production of more reactive species, which photosensitized more dyes molecules (Mukthar and Yesodha 2016). When the MoS_2 NPs were deposited onto the RGO aerogel/ TiO_2 via physical vapor deposition, the resulting RGO aerogel/ $\text{TiO}_2/\text{MoS}_2$ composite showed considerably higher photocatalytic performance because the MoS_2 alone absorbed photons in the visible light region, which produced excited species that generated additional electron-hole pairs for improving photocatalysis. At the end of photocatalytic degradation of RhB (after 120 min), the reaction solution was analyzed by GC-MS. The electron donor and acceptor groups (diethylanilines and carboxylic acid, respectively) in RhB could be easily oxidized by free radicals generated during the photocatalytic process, which resulted in the formation of some colorless organic intermediates that decomposed into smaller organic oxidation products. Based on the GC-MS results in Table S1, it was indicated that the structure of RhB had been degraded.

3.2.3 Performance of the aerogel composites

The removal efficiency of RhB from solution by the RGO aerogel/TiO₂/MoS₂ composite was compared to the corresponding performance of the RGO non-aerogel/TiO₂/MoS₂ (Fig. 7A). The RGO aerogel/TiO₂/MoS₂ demonstrated a stronger adsorption capacity and higher photocatalytic degradation efficiency than the RGO non-aerogel-based composite. This was attributed to the uniformly distributed TiO₂ NPs throughout the surface of the RGO aerogel sheets in the RGO aerogel/TiO₂/MoS₂ composite (Fig. 7B and D, inset), which manifested larger interlayer pores and a higher specific surface area compared to the non-aerogel samples, as observed in the SEM images (Fig. 7B and D). The N₂ adsorption-desorption isotherms (Fig. 7C) of the aerogel and non-aerogel composites, both of which exhibited a type IV isotherm and hysteresis loops similar to the H3 type, further confirmed that the interlayer pores were formed in the stacked sheet-like materials (Li et al. 2013; Lin et al. 2019). The number of pores in the RGO aerogel/TiO₂/MoS₂ was significantly higher than in the RGO non-aerogel/TiO₂/MoS₂ composite, and the pore diameters were larger in the RGO aerogel-based composite compared to the non-aerogel-based composite (inset, Fig. 7C). The large number of mesopores and macropores facilitated the transfer of photons to the internal surface of the catalyst, thereby improving its photoelectric performance. In addition, the BET surface area of the aerogel-based composite was nearly 4.5 times larger than the non-aerogel composite (Table 2). A high specific surface area entails more surface active sites, which improves the carrier mobility rate, adsorption capacity, and photocatalytic performance of the photocatalyst (Li et al. 2013). In addition, a strong adsorption capacity causes more dye molecules to be concentrated at the catalyst surface, thereby increasing the probability of collisions between the dye molecules and reactive species at the surface active sites of the photocatalyst under visible light. Based on these considerations and the removal performances measured, the RGO aerogel/TiO₂/MoS₂ demonstrated a superior removal performance .

Table 2

BET special surface area, pore volume, and average pore size of the two multi-component composites

Samples	BET special surface area (m ² /g)	Pore volume (cm ³ /g)	Average pore size (nm)
RGO aerogel/TiO ₂ /MoS ₂	255.441	1.19565	11.694
RGO non-aerogel/TiO ₂ /MoS ₂	56.953	0.18806	12.465

3.2.4 Removal application of different organic dyes

The removal performance of additional cationic dyes (e.g., Rhodamine B (RhB), crystal violet (CV), and methylene blue (MB)) and anionic dyes (e.g., Alizarin red (AR), xlenol orange (XO), and methyl orange (MO)) by the RGO aerogel/TiO₂/MoS₂ composite was studied (Fig. 8). The removal efficiencies of MB, CV, and RhB by the RGO aerogel/TiO₂/MoS₂ composite were all around 97 %, which were attributed to the presence of negatively charged carboxylate groups on the surface of the RGO aerogel (Fig. 1C). In aqueous solution, the carboxylic acids ionized to generate a large number of negatively charged carboxylates, which enhanced the electrostatic interactions between the catalyst and the cationic dyes

and repelled the anionic dyes. The high removal efficiencies were also facilitated by hydrogen bonding interactions formed between the functional groups of the catalyst and the dyes, which increased the adsorption capacity of the dyes onto the catalyst. Moreover, under strong adsorption, more dye molecules were attached to the surface of the catalyst, making fast and efficient contact between dye molecules and short-lived reactive species generated on the photocatalyst surface (Luo et al. 2019).

In addition, the degradation experiment of the RGO aerogel/TiO₂/MoS₂ composite material in simulated real dye wastewater (Fig. S2), the degradation of anion dye MO under acidic conditions (Fig. S4) and the degradation experiment of the antibiotic tetracycline hydrochloride by the RGO aerogel/TiO₂/MoS₂ composite material (Fig. S5) were also added. The results show that the composite has good degradation performance in simulating the real dye wastewater environment, under acidic conditions, the composite material has a good adsorption effect on the anion dye MO, but the photocatalytic effect is not obvious, and the composite material also has a certain degradation effect on tetracycline hydrochloride.

The corresponding photodegradation kinetics were fairly consistent with a pseudo-first-order reaction (Fig. 8B), and the apparent rate constants calculated for MR, XO, MO, MB, CV, and RhB are shown in Table 3. The apparent rate constants for the photodegradation of the cationic dyes were significantly higher than those of the anionic dyes. The various noncovalent interactions between the cationic dyes and the negatively charged carboxyl groups in the composite can improve the specific surface area, dispersion, and stability of the material, as well as increase the layer spacing. These features provided the RGO aerogel/TiO₂/MoS₂ composite with an excellent adsorption capacity for cationic organic dyes, and made the dye molecules on the surface of the catalyst concentration, in order to realize the dye removal. These results indicated that the RGO aerogel/TiO₂/MoS₂ composite was very effective for the removal of cationic organic dyes from solution.

Table 3
Apparent rate constants (k_{app}) and regression coefficients (R^2) of photodegradation of the six cationic and anionic organic dyes tested.

Organic dye	k_{app} (min ⁻¹)	R^2
AR	0.0014	0.9998
XO	0.0017	0.9973
MO	0.0007	0.9981
MB	0.0167	0.9999
CV	0.0099	0.9945
RhB	0.0169	0.9997

3.2.5 Reusability of the RGO aerogel/TiO₂/MoS₂ composite

The photocatalytic degradation performance of RhB by the composite catalyst for under HPSL irradiation was repeatedly tested to evaluate the reusability of the photocatalyst. The reusability tests were performed five times under the same conditions. After each test, the catalyst was filtered and washed three times with ethanol and three times with deionized water. The catalyst was dried in a vacuum oven at 80°C for 12 hours until the next round of tests. The RGO aerogel/TiO₂/MoS₂ was subjected to five separate cycles of the photocatalytic experiments under HPSL radiation (Fig. 9). After the five cycles were completed, the degradation efficiency of RhB by the photocatalyst decreased from 95–80%. The photodegradation efficiency of the composite catalyst under HPSL radiation decreased because, after each test, the number of active sites on the surface of the catalyst that were responsible for capturing photons decreased, which decreased the ability of the photocatalyst to degrade the organic dyes.

3.2.6 Elucidation of the mechanism of removal of cationic dyes by the composite

During photodegradation, the short-lived reactive species, which included superoxide radicals (O₂^{•-}), holes (h⁺), and hydroxyl radicals (•OH), generated at the surface active sites of the photocatalyst reacted with the dye molecules to degrade them. EPR was performed to detect the O₂^{•-} and •OH species using 5,5-dimethyl-1-pyrroline *N*-oxide (DMPO) as a scavenger. In this EPR assessment, water was introduced for •OH detection, while dimethyl sulfoxide (DMSO) was introduced for O₂^{•-} detection. No EPR signals were observed in the dark; however, under visible light irradiation, four characteristic signals corresponding to the •OH-DMPO adducts were observed in the EPR spectra (Fig. 10A (a)), while six characteristic signals corresponding to the O₂^{•-}-DMPO adducts were observed in the EPR spectra (Fig. 10A (b)) (Wang et al. 2014; Zhang, Junlong et al. 2017). The EPR signal of O₂^{•-} was much stronger than the EPR signal of •OH under irradiation by visible light for 10 min. Due to the valence band (VB) energies of MoS₂ (~ 1.39 eV vs. normal hydrogen electrode (NHE)) (Mukthar and Yesodha 2016) and the RGO aerogel (~ 1.20 eV vs. NHE) (Fig. 9B), neither of the two species could directly oxidize the water or hydroxide ions (OH⁻) to •OH (~ 1.99 eV for OH⁻/•OH and 2.33 eV for H₂O/•OH) (Li et al. 2016; Xia et al. 2019; Zhang, Junlong et al. 2017). Therefore, the observed •OH was generated from the O₂^{•-} or holes produced in the VB of TiO₂ by the photochemical reaction.

To further confirm the contribution of the reactive species to photodegradation, the photocatalytic degradation of RhB using different scavengers was performed by the RGO aerogel/TiO₂/MoS₂ composite under HPSL irradiation (Fig. 10C). Benzoquinone (BQ) was found to inhibit the photocatalytic degradation efficiency of RhB by the RGO aerogel/TiO₂/MoS₂ composite when it was added to scavenge the O₂^{•-} in the solution, which indicated that O₂^{•-} was the essential active species in these photocatalytic degradation reactions. When triethanolamine (TEA) and tert-butyl alcohol (TBA) were added to scavenge the h⁺ and •OH, respectively, the photocatalytic degradation efficiency of RhB by the RGO aerogel/TiO₂/MoS₂ composite was slightly lower than without any scavenger present, meaning h⁺ had a

slight influence on the photocatalytic performance, and low amounts of $\cdot\text{OH}$ were produced (Li et al. 2017; Zhang et al. 2016). These consequences were consistent with the EPR analysis.

Considering the 3D sandwich network structure of the RGO aerogel/ TiO_2 / MoS_2 composite (Fig. 11A), as well as the above results and analyses, a potential adsorption mechanism was proposed (Fig. 11B). The 3D sandwich network composite had a large specific surface area (Table 2) and a significant number of negatively charged carboxylate groups on the surface of the RGO aerogel (Seen in IR, XPS), which enabled the formation of the electrostatic and hydrogen bonding interactions between the composite and the cationic dyes. These interactions provided the composite photocatalyst with a superior absorption capacity for cationic organic dyes (Fig. 8), causing the dye molecules to be removed from solution and concentrated on the surface of the catalyst (Fig. 11B). According to the above results, a potential mechanism for the electron-hole migration was developed (Fig. 11C).

The MoS_2 (Li et al. 2018; Mukthar and Yesodha 2016; Wang et al. 2016), RGO (Li et al. 2016), RGO aerogel/ TiO_2 containing Ti-O-C bonds (Geng et al. 2013; Wang et al. 2017), and RhB (Mukthar and Yesodha 2016) all absorbed visible light, and the excited electrons generated from photon absorption were transferred from the excited RhB (RhB^*) species to the conduction band (CB) of TiO_2 , MoS_2 , and the RGO semiconductor; from the CB of MoS_2 to the CB of TiO_2 and the RGO semiconductor/conductor; and from the CB of the RGO semiconductor to its conductor. The transferred electrons were trapped on the surface of the catalyst by oxygen, producing $\text{O}_2^{\cdot-}$. The reactive oxygen species $\text{O}_2^{\cdot-}$, as well as $\cdot\text{OH}$ generated from the $\text{O}_2^{\cdot-}$, reacted with RhB causing it to degrade. Meanwhile, the corresponding generated holes reacted with RhB to produce organic decomposition intermediates, while the RGO/ TiO_2 material reacted with H_2O to generate $\cdot\text{OH}$, which reacted with the RhB decomposition products to further degrade them. Additionally, the holes within the VBs of the RGO, MoS_2 , and TiO_2 were transferred, which increased the separation of electron-hole pairs.

During the removal of the dyes from solution by the RGO aerogel/ TiO_2 / MoS_2 composite, the adsorption of the dye molecules onto the surface of catalyst facilitated reactions between in fast and efficient contact between the reactive species in solution and the dye molecules, which promoted the degradation of the dyes. Therefore, the combination of adsorption and photocatalytic degradation of RhB and the other cationic organic dyes promoted the efficient removal of the dyes from solution and the subsequent regeneration of the adsorption sites to enable the continuous absorption of dyes onto these regenerated sites. This allowed the RGO aerogel/ TiO_2 / MoS_2 composite to boast excellent removal and photodegradation performances.

Conclusion

RGO aerogel/ TiO_2 / MoS_2 has been prepared using the sol-gel and PVD methods. SEM and TEM results indicate that a unique 3D sandwich network structure has formed by a stepwise hierarchical assembly integration method. BET results show that RGO aerogel/ TiO_2 / MoS_2 composites show high photocatalytic

performance because of its high specific surface area and high adsorption capacity for cationic dyes. Under the combined effect of adsorption and photocatalysis, RGO aerogel/TiO₂/MoS₂ composite exhibits excellent removal performance for high-concentration dye wastewater under visible light irradiation, and the removal rate reaches up to 95% after 2.5 h. This composite material may be regarded as one of the ideal photocatalysts for the treatment of high-concentration dye wastewater.

Declarations

Acknowledgements

The authors acknowledge partial support from the National Natural Science Foundation of China (51874223), the Natural Science Major Research Plan in Shaanxi Province, China (2017ZDJC-25), the Shaanxi Key Laboratory of Environmental Engineering at the Xi'an University of Architecture and Technology, and the Key Laboratory of Northwest Water Resource, Environment and Ecology, MOE, Natural Science Foundation of Shaanxi Province (2020JM-491).

Credit author statement

Liang Zhang, Lvling Zhong, and Xiaomin Zhang conceptualized the study. Liang Zhang acquired the funding. Liang Zhang and Yao Wang supervised the work. Juanqin Xue and Lvling Zhong designed the experiments. Haojie Qi, Yage Zheng and Yujuan Zhang performed the experiments. Yujuan Zhang, Haojie Qi, and Xin Wen organized the results. Yujuan Zhang, Haojie Qi, and Liang Zhang analyzed the data. Haojie Qi and Yujuan Zhang wrote the draft manuscript. Liang Zhang and Haojie Qi reviewed and revised the manuscript.

Funding

The authors acknowledge partial support from the National Natural Science Foundation of China (51874223), Natural Science Major Research Plan in Shaanxi Province, China (2017ZDJC-25), Shaanxi Key Laboratory of Environmental Engineering of Xi'an University of Architecture and Technology, and Key Laboratory of Northwest Water Resource, Environment and Ecology, MOE, Natural Science Foundation of Shaanxi Province (2020JM-491).

Author information

Yujuan Zhang^a, Haojie Qi^a, Liang Zhang^{a,b,c}, Yao Wang^b, Lvling Zhong^b, Yage Zheng^b, Xin Wen^b, Xiaomin Zhang^d, Juanqin Xue^b

^a School of Environmental and Municipal Engineering, Xi'an University of Architecture and Technology, Xi'an, Shaanxi, 710055, China

^b School of Chemistry and Chemical Engineering, Xi'an University of Architecture and Technology, Xi'an, Shaanxi, 710055, China

^c Shaanxi Provincial Key Laboratory of Gold and Resource, Xi'an University of Architecture and Technology, Xi'an, Shaanxi, 710055, China

^d School of resources engineering, Xi'an University of Architecture and Technology, Xi'an, Shaanxi, 710055, China

Corresponding authors

Correspondence to Liang Zhang; Yao Wang.

Ethics declarations

I would like to declare on behalf of my co-authors that the work described in this manuscript is original research that has not been published previously, and not under consideration for publication elsewhere, in whole or in part.

Conflict of interest

No conflict of interest exists in the submission of this manuscript and this manuscript has been approved by all authors for publication. All authors consent to participate and consent to be published.

Declaration of interests

The authors declare that they have no known competing financial interests or personal relationships that could have appeared to influence the work reported in this paper.

Consent to participate

Informed consent was obtained from all individual participants included in the study.

Consent to publish

The participant has consented to the submission of the case report to the journal.

Data Availability Statement

All data generated or analysed during this study are included in this published article and its supplementary information files. The datasets used or analysed during the current study are available from the corresponding author on reasonable request.

References

1. Cai Z, Sun Y, Liu W, Pan F, Sun P, Fu J (2017) An overview of nanomaterials applied for removing dyes from wastewater Environ Sci Pollut Res Int 24:15882-15904 <https://doi.org/10.1007/s11356-017-9003-8>

2. Chen L, Bai B (2013) Equilibrium, Kinetic, Thermodynamic, and in Situ Regeneration Studies about Methylene Blue Adsorption by the Raspberry-like TiO_2 @yeast Microspheres Industrial & Engineering Chemistry Research 52:15568-15577 <https://doi.org/10.1021/ie4020364>
3. Dursun S, Koyuncu SN, Kaya İC, Kaya GG, Kalem V, Akyildiz H (2020) Production of CuO-WO_3 hybrids and their dye removal capacity/performance from wastewater by adsorption/photocatalysis Journal of Water Process Engineering 36 <https://doi.org/10.1016/j.jwpe.2020.101390>
4. El Mersly L et al. (2021) ZnCr-LDHs with dual adsorption and photocatalysis capability for the removal of acid orange 7 dye in aqueous solution Journal of Science: Advanced Materials and Devices 6:118-126 <https://doi.org/10.1016/j.jsamd.2020.08.002>
5. Feng Q, Mao N, Wu J, Xu H, Wang C, Zhang J, Xie L (2015) Growth of $\text{MoS}_{2(1-x)}\text{Se}_{2x}$ ($x = 0.41-1.00$) Monolayer Alloys with Controlled Morphology by Physical Vapor Deposition ACS Nano 9:7450-7455 <https://doi.org/10.1021/acsnano.5b02506>
6. Geng W, Liu H, Yao X (2013) Enhanced photocatalytic properties of titania-graphene nanocomposites: a density functional theory study Physical Chemistry Chemical Physics 15:6025-6033 <https://doi.org/10.1039/c3cp43720e>
7. Guo N, Liang Y, Lan S, Liu L, Zhang J, Ji G, Gan S (2014) Microscale Hierarchical Three-Dimensional Flowerlike TiO_2 /PANI Composite: Synthesis, Characterization, and Its Remarkable Photocatalytic Activity on Organic Dyes under UV-Light and Sunlight Irradiation The Journal of Physical Chemistry C 118:18343-18355 <https://doi.org/10.1021/jp5044927>
8. Hu X, Lu S, Tian J, Wei N, Song X, Wang X, Cui H (2019) The selective deposition of MoS_2 nanosheets onto (101) facets of TiO_2 nanosheets with exposed (001) facets and their enhanced photocatalytic H_2 production Applied Catalysis B: Environmental 241:329-337 <https://doi.org/10.1016/j.apcatb.2018.09.051>
9. Li Q, Guan Z, Wu D, Zhao X, Bao S, Tian B, Zhang J (2017) Z-Scheme BiOCl-Au-CdS Heterostructure with Enhanced Sunlight-Driven Photocatalytic Activity in Degrading Water Dyes and Antibiotics ACS Sustainable Chemistry & Engineering 5:6958-6968 <https://doi.org/10.1021/acssuschemeng.7b01157>
10. Li W et al. (2013) Sol-gel design strategy for ultradispersed TiO_2 nanoparticles on graphene for high-performance lithium ion batteries Journal of the American Chemical Society 135:18300-18303 <https://doi.org/10.1021/ja4100723>
11. Li X, Yu J, S. Wageh AAA-G, Xie J (2016) Graphene in Photocatalysis: A Review Small 12: 6640-6696 <https://doi.org/10.1002/smll.201600382>
12. Li Z, Meng X, Zhang Z (2018) Recent development on MoS_2 -based photocatalysis: A review Journal of Photochemistry and Photobiology C: Photochemistry Reviews 35:39-55 <https://doi.org/10.1016/j.jphotochemrev.2017.12.002>
13. Li Juan-Juan et al. (2018) Efficient infrared light promoted degradation of volatile organic compounds over photo-thermal responsive Pt-rGO-TiO_2 composites Applied Catalysis B:

- Environmental 233:260–271 <https://doi.org/10.1016/j.apcatb.2018.04.011>
14. Lin Y, Ren P, Wei C (2019) Fabrication of MoS₂/TiO₂ heterostructures with enhanced photocatalytic activity CrystEngComm 21:3439-3450 <https://doi.org/10.1039/c9ce00056a>
 15. Liu X et al. (2017) Fabrication of 3D flower-like black N-TiO₂-x@MoS₂ for unprecedented-high visible-light-driven photocatalytic performance Applied Catalysis B: Environmental 201:119-127 <https://doi.org/10.1016/j.apcatb.2016.08.031>
 16. Luo Y et al. (2019) Synergistic adsorption-photocatalysis processes of graphitic carbon nitrate (g-C₃N₄) for contaminant removal: Kinetics, models, and mechanisms Chemical Engineering Journal 375:122019 <https://doi.org/10.1016/j.cej.2019.122019>
 17. Martins JT, Guimaraes CH, Silva PM, Oliveira RL, Prediger P (2020) Enhanced removal of basic dye using carbon nitride/graphene oxide nanocomposites as adsorbents: high performance, recycling, and mechanism Environ Sci Pollut Res Int <https://doi.org/10.1007/s11356-020-10779-z>
 18. Mukthar AM, Yesodha SKN (2016) One step solvothermal synthesis of carbon doped TiO₂-MoS₂ heterostructure composites with improved visible light catalytic activity New Journal of Chemistry 40:8123-8130 <https://doi.org/10.1039/C6NJ00533K>
 19. Paul KK, Mawlong LPL, Giri PK (2018) Trion-Inhibited Strong Excitonic Emission and Broadband Giant Photoresponsivity from Chemical Vapor-Deposited Monolayer MoS₂ Grown in Situ on TiO₂ Nanostructure ACS Applied Material & Interfaces 10:42812-42825 <https://doi.org/10.1021/acsami.8b14092>
 20. Qiao H, Huang Z, Liu S, Tao Y, Zhou H, Li M, Qi X (2019) Novel Mixed-Dimensional Photocatalysts Based on 3D Graphene Aerogel Embedded with TiO₂/MoS₂ Hybrid The Journal of Physical Chemistry C 123:10949-10955 <https://doi.org/10.1021/acs.jpcc.9b00466>
 21. Quan Quan, Xie Shunji, Weng Bo, Wang Ye, Xu Yi-Jun (2018) Revealing the Double-Edged Sword Role of Graphene on Boosted Charge Transfer versus Active Site Control in TiO₂ Nanotube Arrays@RGO/MoS₂ Heterostructure small 14:1704531 <https://doi.org/10.1002/sml.201704531>
 22. Shi H et al. (2017) Uniform Gold-Nanoparticle-Decorated {001}-Faceted Anatase TiO₂ Nanosheets for Enhanced Solar-Light Photocatalytic Reactions ACS Applied Materials & Interfaces 9:36907-36916 <https://doi.org/10.1021/acsami.7b12470>
 23. Wang C, Meng D, Sun J, Memon J, Huang Y, Geng J (2014) Graphene Wrapped TiO₂ Based Catalysts with Enhanced Photocatalytic Activity Advanced Materials Interfaces 1:1300150 <https://doi.org/10.1002/admi.201300150>
 24. Wang C, Zhan Y, Wang Z (2018) TiO₂, MoS₂, and TiO₂/MoS₂ heterostructures for use in organic dyes degradation ChemistrySelect 3:1713-1718 <https://doi.org/10.1002/slct.201800054>
 25. Wang D, Xu Y, Sun F, Zhang Q, Wang P, Wang X (2016) Enhanced photocatalytic activity of TiO₂ under sunlight by MoS₂ nanodots modification Applied Surface Science 377:221-227 <https://doi.org/10.1016/j.apsusc.2016.03.146>

26. Wang P, Wang J, Wang X, Yu H, Yu J, Lei M, Wang Y (2013) One-step synthesis of easy-recycling TiO₂-rGO nanocomposite photocatalysts with enhanced photocatalytic activity *Applied Catalysis B: Environmental* 132:452-459 <https://doi.org/10.1016/j.apcatb.2012.12.009>
27. Wang P, Zhan S, Xia Y, Ma S, Zhou Q, Li Y (2017) The fundamental role and mechanism of reduced graphene oxide in rGO/Pt-TiO₂ nanocomposite for high-performance photocatalytic water splitting *Applied Catalysis B: Environmental* 207:335-346 <https://doi.org/10.1016/j.apcatb.2017.02.031>
28. Xia P, Cheng B, Jiang J, Tang H (2019) Localized π -conjugated structure and EPR investigation of g-C₃N₄ photocatalyst *Applied Surface Science* 487:335-342 <https://doi.org/10.1016/j.apsusc.2019.05.064>
29. Xin X, Li S-H, Zhang N, Tang Z-R, Xu Y-J (2019) 3D graphene/AgBr/Ag cascade aerogel for efficient photocatalytic disinfection *Applied Catalysis B: Environmental* 245:343–350 <https://doi.org/10.1016/j.apcatb.2018.12.066>
30. Yahia Cherif L, Yahiaoui I, Aissani-Benissad F, Madi K, Benmehdi N, Fourcade F, Amrane A (2014) Heat Attachment Method for the Immobilization of TiO₂ on Glass Plates: Application to Photodegradation of Basic Yellow Dye and Optimization of Operating Parameters, Using Response Surface Methodology *Industrial & Engineering Chemistry Research* 53:3813-3819 <https://doi.org/10.1021/ie403970m>
31. Yang J, Miao H, Wei Y, Li W, Zhu Y (2019) π - π Interaction between self-assembled perylene diimide and 3D graphene for excellent visible-light photocatalytic activity *Applied Catalysis B: Environmental* 240:225-233 <https://doi.org/10.1016/j.apcatb.2018.09.003>
32. Yang S, Wang L, Zhang X, Yang W, Song G (2015) Enhanced adsorption of Congo red dye by functionalized carbon nanotube/mixed metal oxides nanocomposites derived from layered double hydroxide precursor *Chemical Engineering Journal* 275:315–321 <https://doi.org/10.1016/j.cej.2015.04.049>
33. Ye Fei, Li Houfen, Yu Hongtao, Chen Shuo, Quan Xie (2017) Hydrothermal fabrication of few-layer MoS₂ nanosheets within nanopores on TiO₂ derived from MIL-125(Ti) for efficient photocatalytic H₂ evolution *Applied Surface Science* 426:177–184 <https://doi.org/10.1016/j.apsusc.2017.07.087>
34. Zhang J et al. (2016) Hollow Sphere TiO₂-ZrO₂ Prepared by Self-Assembly with Polystyrene Colloidal Template for Both Photocatalytic Degradation and H₂ Evolution from Water Splitting *ACS Sustainable Chemistry & Engineering* 4:2037-2046 <https://doi.org/10.1021/acssuschemeng.5b01359>
35. Zhang L et al. (2019) Au nanoparticle modified three-dimensional network PVA/RGO/TiO₂ composite for enhancing visible light photocatalytic performance *Applied Surface Science* 498:143855 <https://doi.org/10.1016/j.apsusc.2019.143855>
36. Zhang L, Zhao Y, Zhong L, Wang Y, Chai S, Yang T, Han X (2017) Cu₂S-Cu-TiO₂ mesoporous carbon composites for the degradation of high concentration of methyl orange under visible light *Applied Surface Science* 422:1093-1101 <https://doi.org/10.1016/j.apsusc.2017.05.100>

37. Zhang W, Xiao X, Zheng L, Wan C (2015) Fabrication of $\text{TiO}_2/\text{MoS}_2$ @zeolite photocatalyst and its photocatalytic activity for degradation of methyl orange under visible light *Applied Surface Science* 358:468-478 <https://doi.org/10.1016/j.apsusc.2015.08.054>
38. Zhang X, Zong Z, Zhang X, Zhang D, Luo Q, Bi C, Fan Y (2020) Rational design of three bifunctional MOFs for photocatalysis degradation and selective adsorption of wastewater organic dyes removal *Polyhedron* 191 <https://doi.org/10.1016/j.poly.2020.114816>
39. Zhang Junlong et al. (2017) Novel AuPd bimetallic alloy decorated 2D BiVO_4 nanosheets with enhanced photocatalytic performance under visible light irradiation *Applied Catalysis B: Environmental* 204:385-393 <https://doi.org/10.1016/j.apcatb.2016.11.057>
40. Zhou X et al. (2016) High performance near-infrared photodetectors based on ultrathin SnS nanobelts grown via physical vapor deposition *Journal of Materials Chemistry C* 4:2111-2116 <https://doi.org/10.1039/c5tc04410c>

Figures

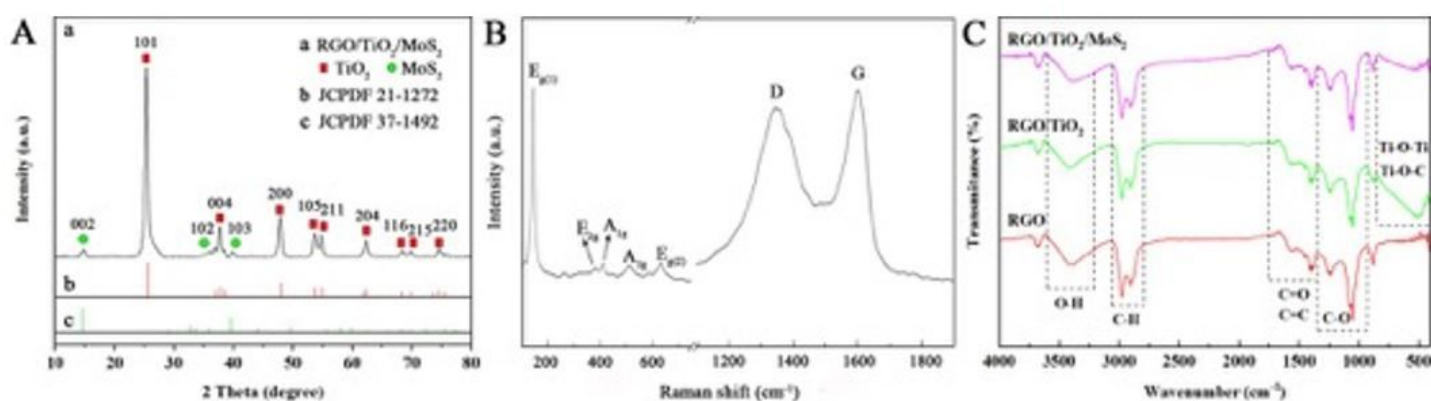


Figure 1

(A) XRD patterns; (B) Raman spectrum of the RGO aerogel/ $\text{TiO}_2/\text{MoS}_2$; and (C) FT-IR spectra of the RGO aerogel/ $\text{TiO}_2/\text{MoS}_2$, RGO aerogel/ TiO_2 , and RGO aerogel.

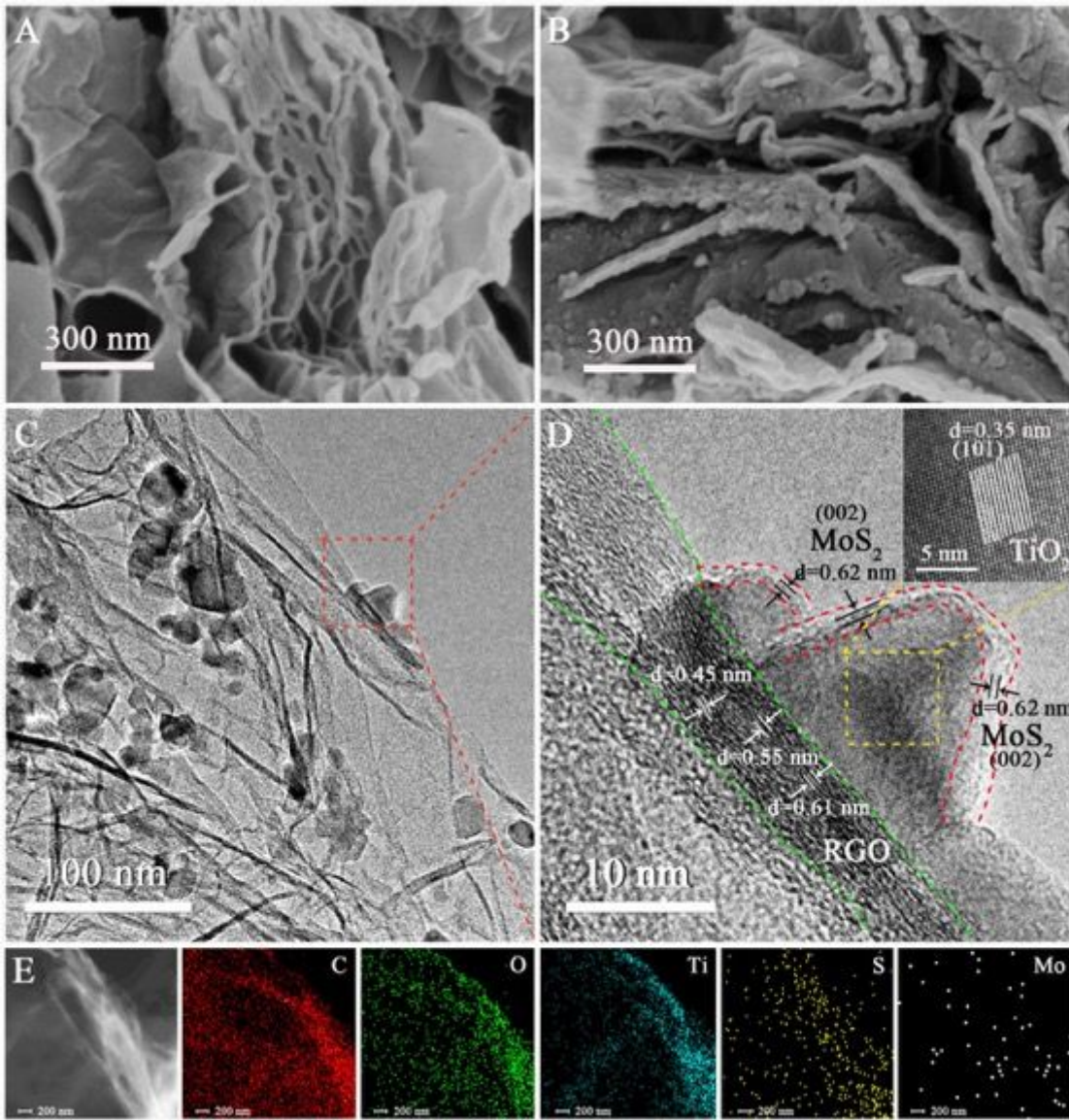


Figure 2

SEM image of (A) RGO aerogel and (B) RGO aerogel/TiO₂/MoS₂. TEM image of RGO aerogel/TiO₂/MoS₂: (C) TEM image, (D) HRTEM image. (E) EDS elemental mapping results from the RGO aerogel/TiO₂/MoS₂ showing C, O, Ti, S, and Mo, respectively.

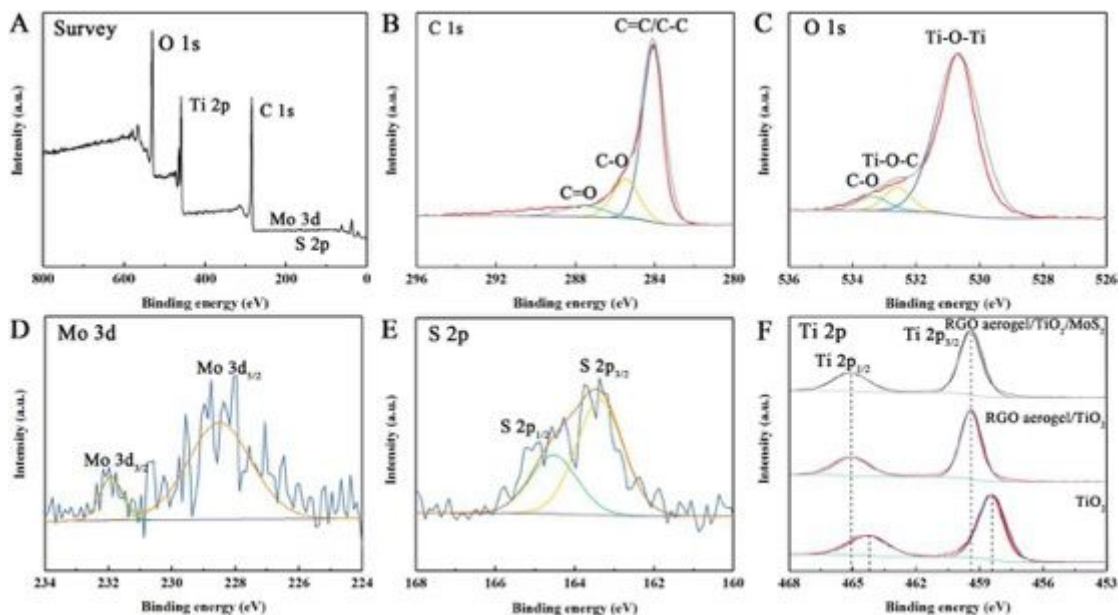


Figure 3

XPS spectra of the RGO aerogel/TiO₂/MoS₂: (A) survey, (B) C 1s, (C) O 1s, (D) Mo 3d, and (E) S 2p; (F) Ti 2p spectra of the TiO₂, RGO aerogel/TiO₂, and RGO aerogel/TiO₂/MoS₂.

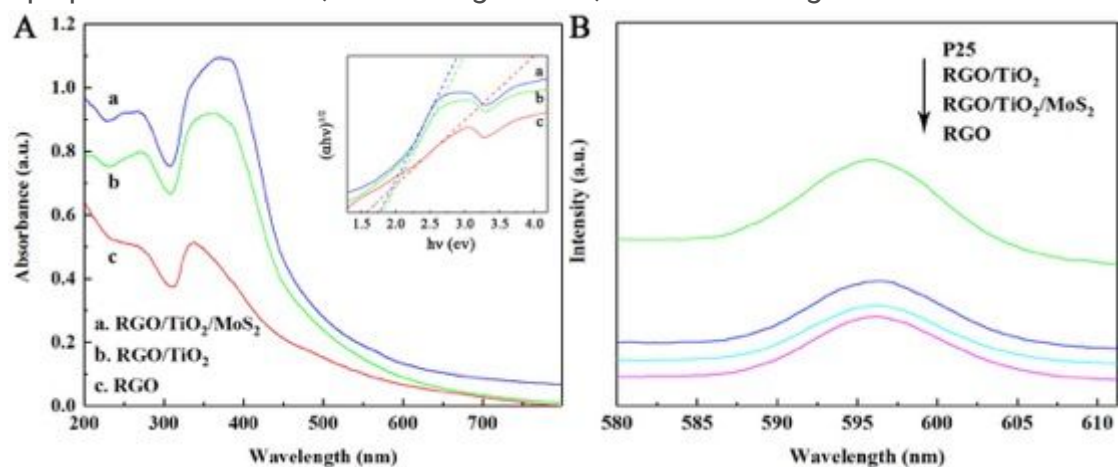


Figure 4

UV-Vis DRS (A) and PL (B) spectra of the RGO aerogel, RGO aerogel/TiO₂, and RGO aerogel/TiO₂/MoS₂ materials. (A) RGO aerogel/TiO₂/MoS₂, (b) RGO aerogel/TiO₂, and (c) RGO aerogel (inset: the plots of the Kubelka-Munk function of the spectra) (B) PL spectra: P25, RGO aerogel, RGO aerogel/TiO₂, and RGO aerogel/TiO₂/MoS₂.

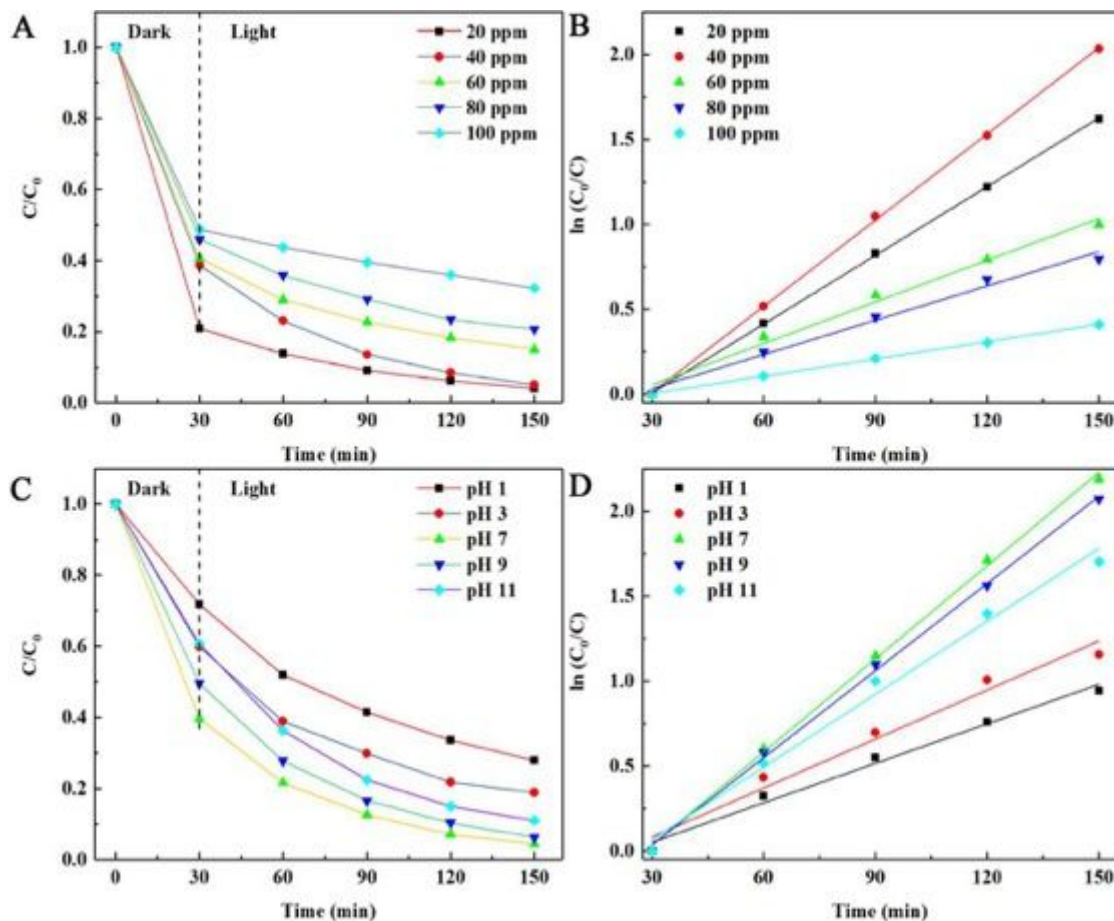


Figure 5

(A) Removal performance of RhB onto the RGO aerogel/TiO₂/MoS₂ composite at different RhB concentrations; (B) photodegradation kinetics of RhB on the RGO aerogel/TiO₂/MoS₂ composite at different RhB concentrations (0.01 g catalyst was used in this experiment at pH 7.0); (C) Removal performance of RhB by the RGO aerogel/TiO₂/MoS₂ composite at different pH's; and (D) the corresponding photodegradation kinetics (80 mL of 40 mg·L⁻¹ RhB and 0.01g catalyst were used in this experiment).

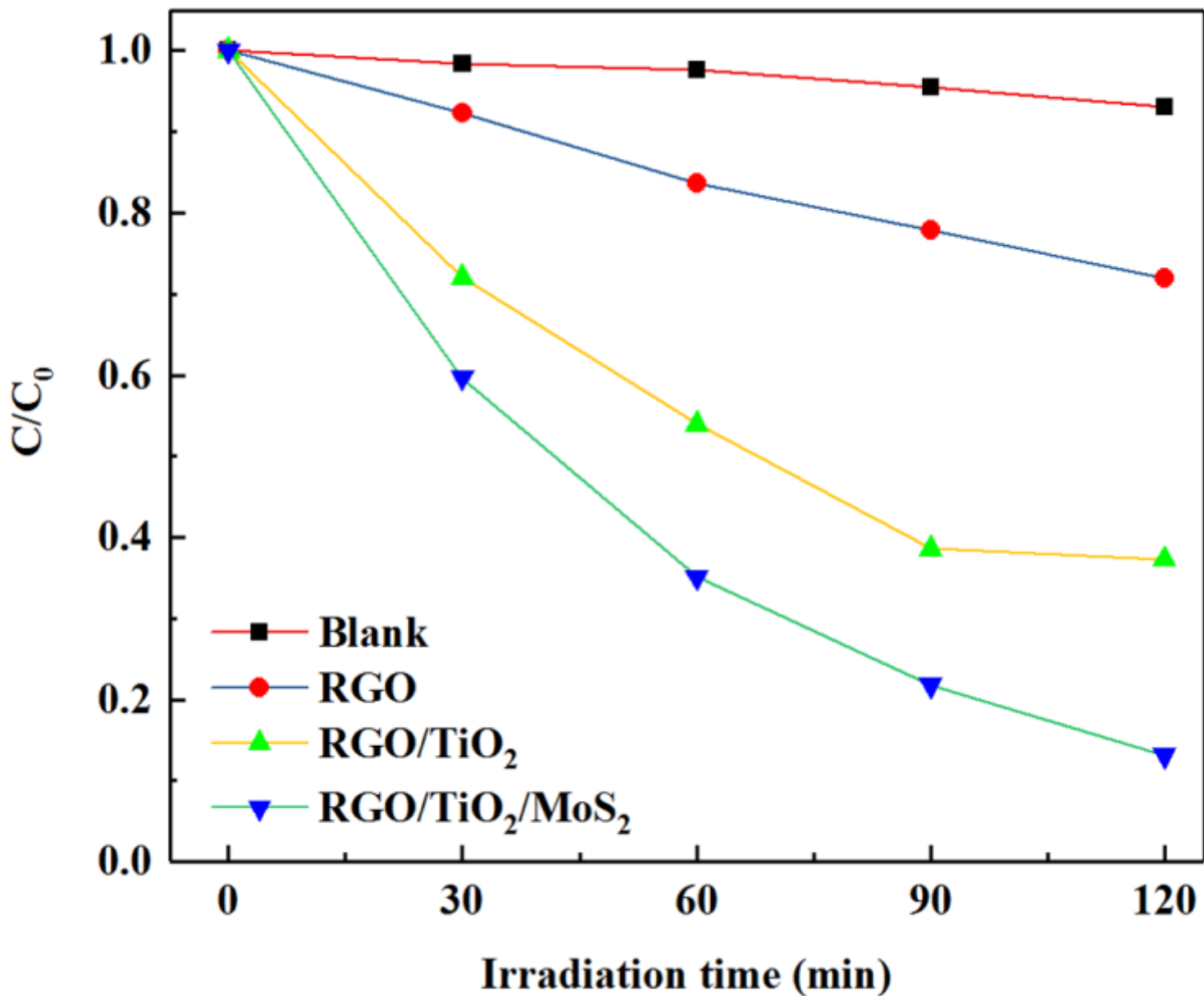


Figure 6

Photocatalytic performance of RhB on the different catalysts under HPSL irradiation. (80 mL of 40 mg·L⁻¹ RhB and 0.01g catalyst at pH 7.0 were used in this experiment. The blank was RhB without added catalyst)

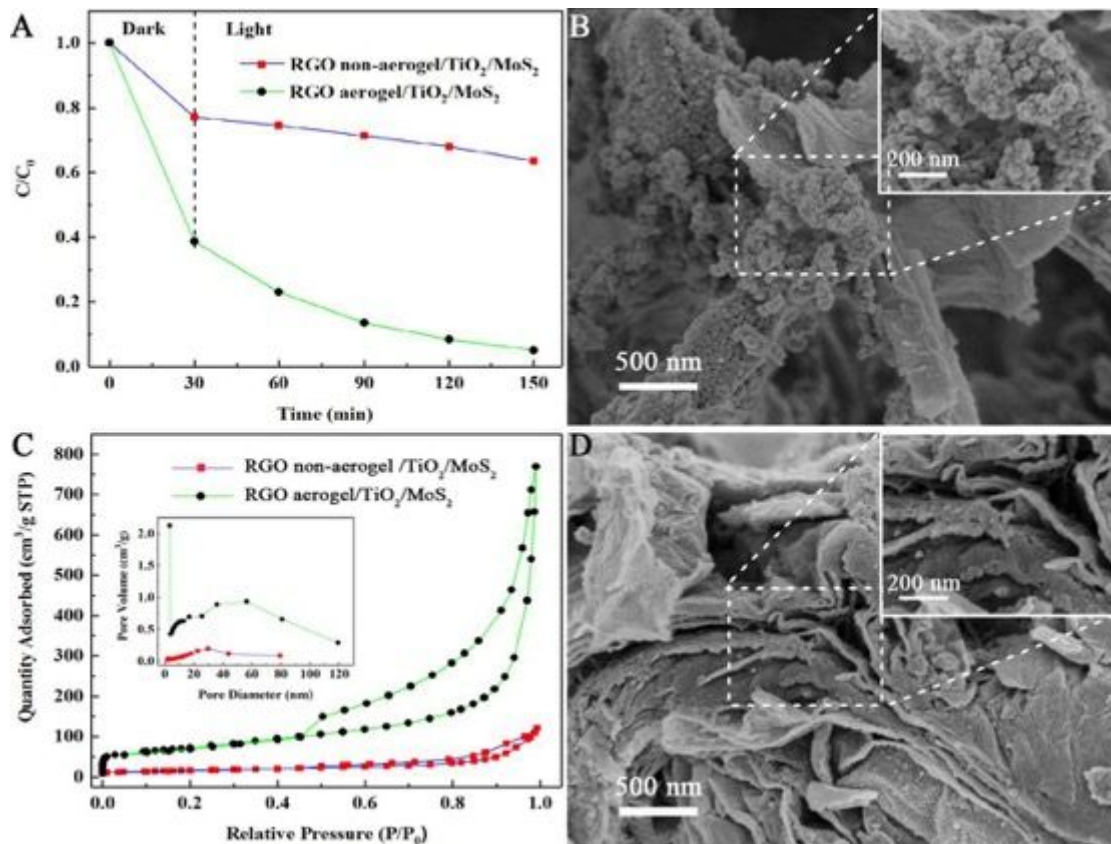


Figure 7

(A) Removal performance of RhB by the RGO non-aerogel/TiO₂/MoS₂ and RGO aerogel/TiO₂/MoS₂ composites (80 mL of 40 mg L⁻¹ RhB and 0.01g catalyst were used in this experiment at pH 7.0); (B) SEM image of the RGO non-aerogel/TiO₂/MoS₂ composite; (C) N₂ adsorption-desorption isotherms of the RGO non-aerogel/TiO₂/MoS₂ and RGO aerogel/TiO₂/MoS₂ composites (inset: pore size distribution curves of the two composites); and (D) SEM image of the RGO aerogel/TiO₂/MoS₂ composite.

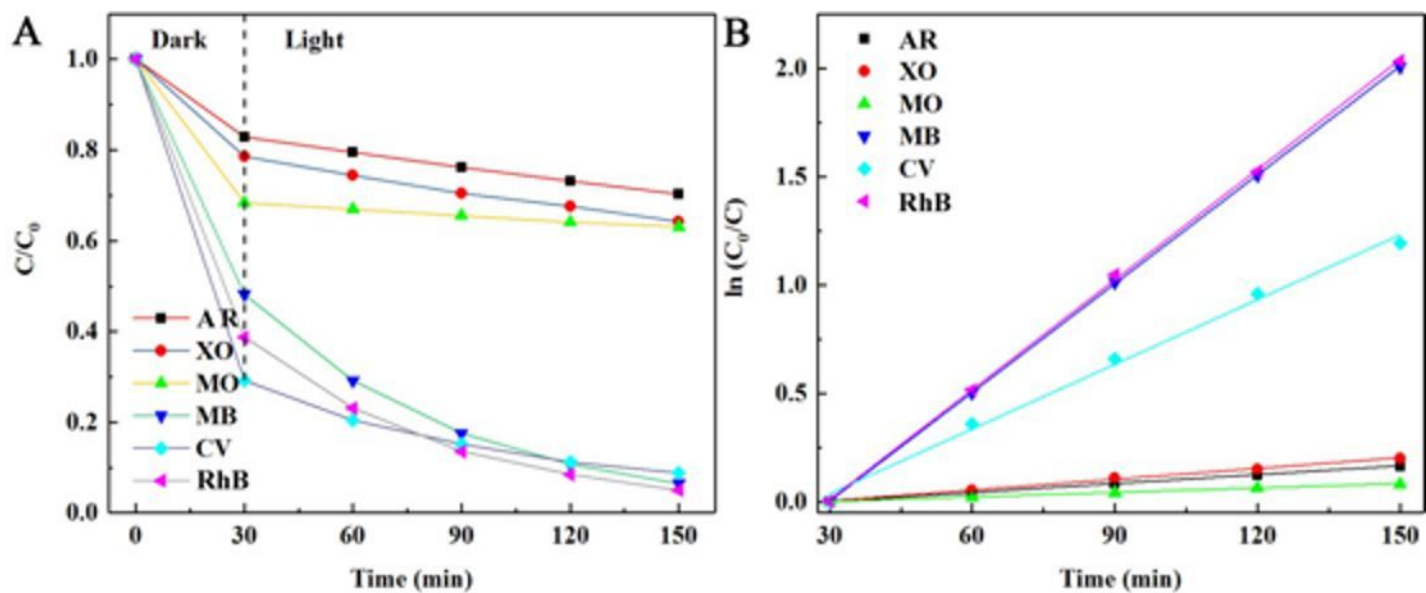


Figure 8

(A) The removal performance of the different organic dyes from solution onto the RGO aerogel/TiO₂/MoS₂ composite, and (B) the corresponding photodegradation kinetics for all dyes. Conditions: 80 mL of 40 mg·L⁻¹ dye solutions and 0.01g catalyst at pH 7.0.

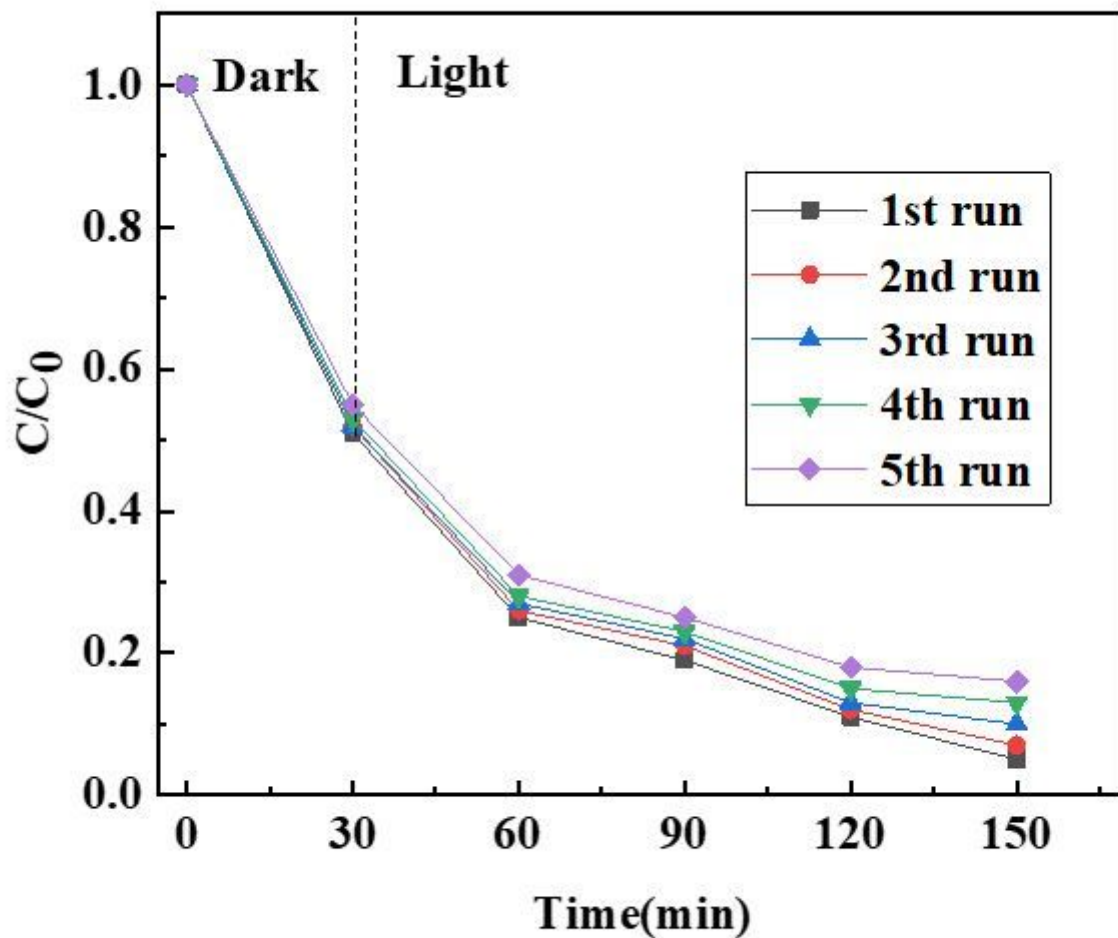


Figure 9

Photocatalytic degradation curves of RhB by the RGO aerogel/TiO₂/MoS₂ photocatalyst (80 mL of 40 mg·L⁻¹ RhB and 0.01g catalyst were used in this experiment at pH 7.0)

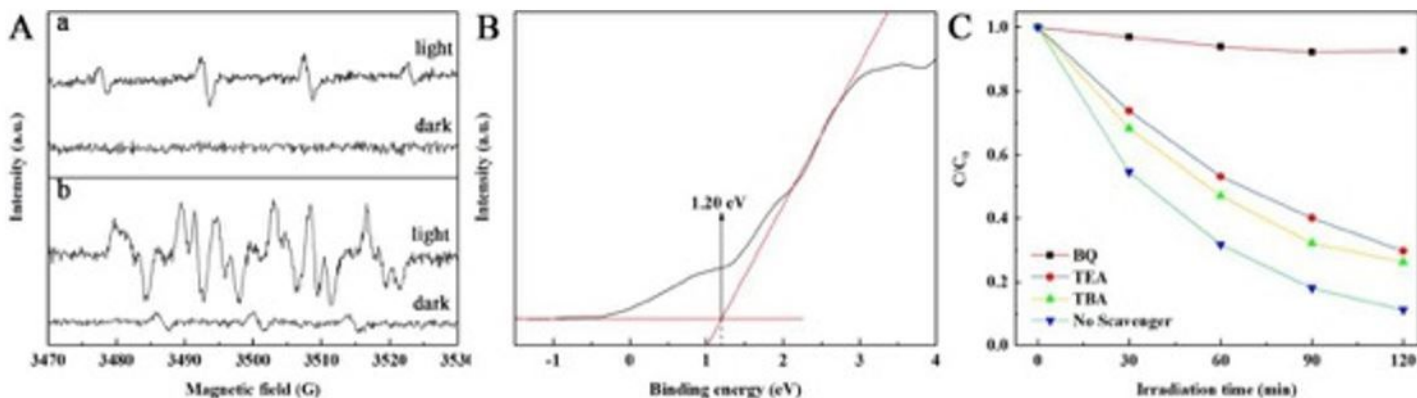


Figure 10

(A) EPR spectra of the RGO aerogel/TiO₂/MoS₂ composite in a water dispersion (a) and DMSO dispersion (b) under visible light irradiation for 10 min. (B) XPS valence-band spectra of the RGO aerogel. (C) The effect of BQ, TEA, and TBA on the photodegradation performance of RhB by the RGO aerogel/TiO₂/MoS₂ composite (80 mL of 40 mg·L⁻¹ RhB and 0.01g catalyst were used in this experiment at pH 7.0)

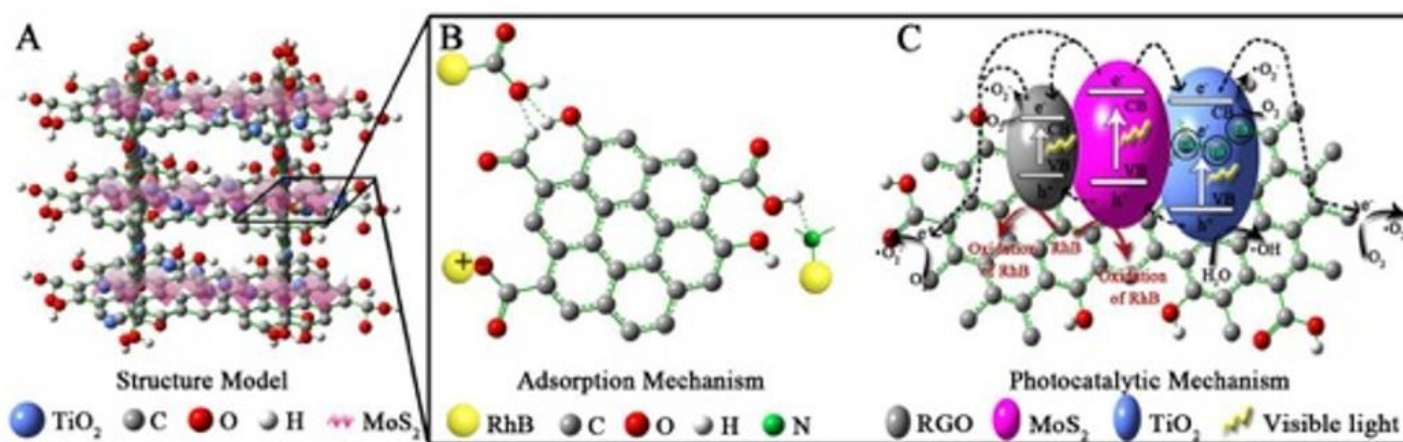


Figure 11

(A) The sandwich structure model of the composite, (B) a proposed mechanism for the adsorption process, and (C) a proposed mechanism for electron-hole migration in the RGO aerogel/TiO₂/MoS₂.

Supplementary Files

This is a list of supplementary files associated with this preprint. Click to download.

- [GraphicalAbstract.docx](#)
- [SupplementaryMaterials.docx](#)